

DEPARTAMENT D' ASTRONOMIA I METEOROLOGIA



UNIVERSITAT DE BARCELONA



Near-relativistic electron events.
Monte Carlo simulations of solar
injection and interplanetary transport

Memòria presentada per
Neus Àgueda Costafreda
per optar al grau de Doctora
per la Universitat de Barcelona.
Barcelona, 20 de febrer de 2008

2 Instrumentation and data analysis

2.1 The Advanced Composition Explorer

The *Advanced Composition Explorer (ACE)* spacecraft was launched on 1997 August 25 with the prime objective of determining and comparing the elemental and isotopic composition of distinct samples of matter, including the solar corona, the interplanetary medium, the local interstellar medium, and the galactic matter. The *ACE* mission was overseen by the US National Aeronautics and Space Administration (NASA) at the Goddard Space Flight Center¹. The development, integration and test of the spacecraft was assigned to The Johns Hopkins University Applied Physics Laboratory (JHU/APL). Science payload management and the online processing and distribution of the data were the responsibilities of the California Institute of Technology^{2,3}.

ACE was launched carrying six high-resolution sensors and three monitoring instruments to sample low-energy particles of solar origin and high-energy galactic particles with a collecting power 10 to 1000 times greater than past experiments. The properties of the nine experiments are summarized in Table 2.1. In particular,

- CRIS measures the elemental and isotopic composition of galactic cosmic rays over the energy range from ~ 100 to $600 \text{ MeV nucl}^{-1}$ (Stone et al. 1998a).
- SIS measures the elemental and isotopic composition of energetic nuclei from 10 to 100 MeV nucl^{-1} (Stone et al. 1998b). The energy range covered by SIS includes transient fluxes of energetic nuclei accelerated in large solar particle events, as well as anomalous cosmic rays and low-energy galactic cosmic rays.
- ULEIS measures the mass and kinetic energy of nuclei from He to Ni (Mason et al. 1998). The energy range covered by ULEIS includes SEPs, particles accelerated by interplanetary shocks and low-energy anomalous cosmic rays.

¹http://helios.gsfc.nasa.gov/ace/ace_mission.html

²<http://www.srl.caltech.edu/ACE/>

³<http://www.srl.caltech.edu/ACE/ASC/>

- SEPICA measures the charge state, kinetic energy, and the nuclear charge of energetic ions from ~ 0.2 to 3 MeV nucl^{-1} (Möbius et al. 1998). Measurements of SEP charge states provide information on the temperature and/or density of the source plasma, as well as possible charge-to-mass dependent acceleration processes.
- EPAM characterizes the dynamic behavior of electrons and ions with ~ 0.03 to 5 MeV that are accelerated by impulsive solar flares and by interplanetary shocks associated with CMEs and corotating interaction regions (CIRs) (Gold et al. 1998). EPAM was developed from the flight spare of the HI-SCALE instrument flown on *Ulysses*.
- SWIMS is a spectrometer that measures solar wind isotopic composition in all solar wind conditions (Gloeckler et al. 1998). The design is based on that of similar instruments on *Wind* and *SOHO*.
- SWICS is a spectrometer that determines the elemental and ionic charge state composition of all major solar wind ions from H to Fe using a combination of electrostatic deflection, post-acceleration, time-of-flight, and energy measurements (Gloeckler et al. 1998). SWICS is the flight spare of an essentially identical instrument flown on *Ulysses*, where it has been particularly useful for measuring the characteristics of solar wind pickup ions.
- SWEPEM measures the three-dimensional characteristics of solar wind and suprathermal electrons from ~ 1 to 900 eV and ions from 0.26 to 35 keV (McComas et al. 1998). It consists of modified versions of the spare solar wind electron and ion sensors from the *Ulysses* mission.
- MAG measures the dynamic behavior of the magnetic field vector, including measurements of interplanetary shocks and waves, as well as other features that govern the acceleration and transport of energetic particles (Smith et al. 1998). MAG is a flight spare of the magnetometer instrument flown on *Wind*.

In order to avoid the effects of the Earth's magnetic field, the *ACE* spacecraft was located at the Sun-Earth libration point (L1) - a point of Earth-Sun gravitational equilibrium about 1.5 million kilometers from Earth and 148.5 million kilometers from the Sun. By orbiting the L1 point, *ACE* stays in a relatively constant position with respect to Earth. From this location, *ACE* can measure the solar wind, the interplanetary magnetic field and SEPs accelerated close to the Sun and in the heliosphere. *ACE* has been at the L1 point for 10 years and the spacecraft and instruments are still working very well, with the exception of the SEPICA instrument. The spacecraft has enough propellant on board to maintain an orbit at L1 until ~ 2022 .

Table 2.1: ACE instrumentation

Sensor	Full name	Measured species	Measured quantities	Typical energy (MeV nucl^{-1})
CRIS	Cosmic-ray isotope spectrometer	$2 \leq Z \leq 30$	Z, M, E	~ 200
SIS	Solar isotope spectrometer	$2 \leq Z \leq 30$	Z, M, E	~ 20
ULEIS	Ultra low energy isotope spectrometer	$2 \leq Z \leq 28$	M, E	~ 1
SEPICA	Solar energetic particle ionic charge analyzer	$2 \leq Z \leq 28$	Q, Z, E	~ 1
EPAM	Electron, proton and alpha monitor	H, He, e^-	Z, M, E	~ 0.3
SWIMS	Solar wind ion mass spectrometer	$2 \leq Z \leq 30$	$M, E/Q$	~ 0.001
SWICS	Solar wind ion composition spectrometer	$2 \leq Z \leq 30$	Z, E	~ 0.001
SWEPAM	Solar wind electron, proton and alpha monitor	H, He	E/Q dist.	~ 0.001
MAG	Magnetometer	B	B_x, B_y, B_z	

E = energy, M = mass, Z = nuclear charge, Q = ion charge, B = magnetic field.

ACE is a spin-stabilized spacecraft and several of its instruments use the spinning of the spacecraft to scan the sky. The spin axis of the cylindrically shaped spacecraft generally points within 20° of the Sun. The spin period of the spacecraft is of 12 s (5 rpm).

2.2 The EPAM experiment. Data sets

The Electron, Proton, and Alpha Monitor (EPAM) was designed to measure ions and electrons in the energy range from about 50 keV to 5 MeV (Gold et al. 1998). It consists of five solid-state detector systems on two stub telescopes. Each stub telescope supports a Low-Energy Magnetic Spectrometer (LEMS) and a Low-Energy Foil Spectrometer (LEFS). These two detector systems together form a LEMS/LEFS pair, which is identical in design on each stub-arm telescope. The two LEMS sensors are oriented 30° and 120° from the spin axis and are identified as LEMS30 and LEMS120 telescopes. The LEFS detectors are pointed 60° and 150° from the spacecraft spin axis and are known as the LEFS60 and LEFS150 telescopes. The last detector system measures ion composition and is referred to as the Composition Aperture (CA). Since its look direction is oriented 60° from the spacecraft spin-axis, it is known as the CA60 telescope.

As the *ACE* spacecraft spins, these five telescopes sweep out swaths of space, provid-

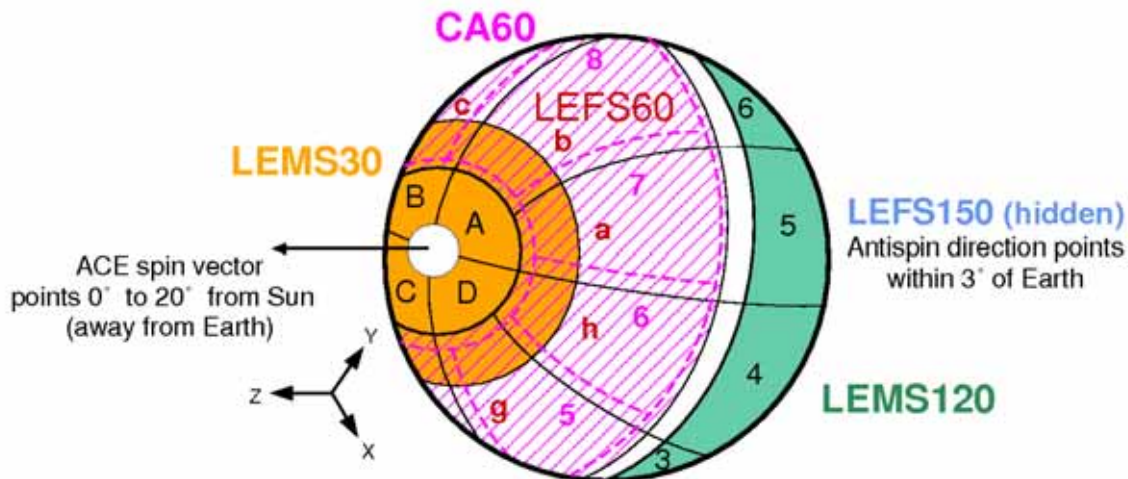


Figure 2.1: The five EPAM detector assemblies projected onto the unit sphere and the approximate definition of the sectors (from Gold et al. 1998).

ing nearly full three-dimensional coverage for measuring ion anisotropies and approximately 40% coverage for electron anisotropies (Gold et al. 1998). As the spacecraft spins, the instrument electronics sample the detectors such that the swath of space swept out by each telescope is divided into nearly equally spaced sectors. In the case of the detector pair, LEMS30/LEFS150, four sectors are used, each 90° wide. On the other hand, the LEMS120-/LEFS60 detector pair is divided into eight sectors, each 45° wide. Figure 2.1 illustrates the look directions of the five EPAM telescopes projected onto the unit sphere as well as the approximate definitions of their sectors.

Of particular interest to this study are two of the electron telescopes, namely, LEFS60 and LEMS30. The LEFS60 telescope measures energetic (0.046–4.9 MeV) ions and NR (45–312 keV) electrons in seven energy channels (four for electrons and three for ions). An aluminized Parylene foil, nominally 0.35 mg cm^{-2} thick, absorbs ions with energies below 350 keV while it allows electrons with energies above 45 keV to pass through a solid-state detector. The geometric factor of the LEFS60 telescope is $0.397 \text{ cm}^2 \text{ sr}$ and it has a full-cone opening angle of 53° . Table 2.2 lists the passbands of the LEFS60 energy channels.

The LEMS30 telescope measures energetic (0.047–4.75 MeV) ions and NR (38–315 keV) electrons in twelve energy channels (four for electrons and eight for ions). The LEMS30 detector is a 200 micron, totally depleted, solid-state silicon surface barrier detector with geometric factor $0.428 \text{ cm}^2 \text{ sr}$. A rare-earth magnet in front of the LEMS30 detector sweeps out any electrons with energy below about 500 keV. These electrons are measured in the *B* detector referred as DE30 (Deflected Electrons). The DE30 detector measures pure electrons with a geometric factor of $0.140 \text{ cm}^2 \text{ sr}$ within a full-cone opening angle of 51° . The DE

Table 2.2: EPAM electron channels

EPAM system	Channel	Energy (keV)	Speed ($\times c$)	Geometric factor (cm^2sr)
LEFS60	E'1	045–062	0.42	0.397
LEFS60	E'2	062–102	0.50	0.397
LEFS60	E'3	102–175	0.61	0.397
LEFS60	E'4	175–312	0.73	0.397
LEMS30	DE1	038–053	0.39	0.140
LEMS30	DE2	053–103	0.49	0.140
LEMS30	DE2	103–175	0.62	0.140
LEMS30	DE2	175–315	0.73	0.140

channels, energy passbands, and velocities are given in Table 2.2.

Unfortunately, the LEFS60 telescope and the DE30 detector are not cross calibrated. This makes it difficult to use data from the two electron telescopes in a joined quantitative analysis. We choose LEFS60 electron data for a further analysis because the LEFS60 telescope has a better angular resolution than the LEMS30 telescope (it is divided into more sectors). In addition, the LEFS60 particle detector has a larger geometric factor than DE30 and, therefore, it is statistically more accurate.

Contamination from ions, however, is possible in the LEFS60 data. Therefore, we qualitatively compare DE30 electron measurements to LEFS60 data. When data is not contaminated, we expect similar trends in the electron spin-averaged profiles observed by the two telescopes; small differences may be caused by the fact that the two telescopes sweep different regions of space.

In this thesis, we analyze 72 s averages of the sectorized electron intensities measured by the LEFS60 telescope in the energy range 62–312 keV. Haggerty & Roelof (2003) determined the secondary responses for the LEMS30 deflected electron channels (close to those of LEFS60) and found that DE2 and DE3 channels have strong responses to electrons of $\gtrsim 300$ keV and $\gtrsim 250$ keV, respectively. They found that the effect depends on the spectral slope of the event: it is noticeable for $\gamma < 4$ and severe for $\gamma < 2$. Therefore, because of possible contribution from higher energy electrons, we exclude the lowest energy channel of the LEFS60 telescope (45–62 keV) from a further analysis.

For completion, we also use 8 min spin-averaged P'7 (1.06–1.90 MeV) and P'8 (1.90–4.80 MeV) proton intensities observed by the LEMS120 telescope and 72 s spin-averaged 53–315 keV electron intensities observed by the DE30 detector.

2.3 Other observational data

We make use of 8 min 1.33–4.75 MeV spin-averaged proton intensities observed by the Energetic and Relativistic Nuclei and Electron (ERNE) experiment on board *SOHO* (Torsti et al. 1995), to compare with those observed by EPAM/LEMS120. The LEMS120 telescope is oriented 120° with respect to the spin axis, thus its look direction is opposite to the Sun. In contrast, ERNE measures particle intensities coming from the Sun within a limited field of view aligned with the nominal Parker field direction. Although these two instruments are not cross-calibrated, their measurements can be compared in order to obtain a precise estimation of the onset of the proton event and therefore, to discern whether the proton intensities measured by LEMS120 are contaminated by other species. ERNE particle intensity measurements can be downloaded from the ERNE Datafinder web page⁴. We use 8 min spin-averaged intensities measured in the 1.33–1.90 MeV and 1.90–4.75 MeV energy channels to compare with P’7 and P’8 energy channels from the LEMS120 telescope.

We use ground-based observations reported by the Solar Geophysical Data (SGD; US DoC)⁵ to identify the location of H α flares associated with the NR electron events observed by *ACE*. SGD also provides a list of the associated X-ray flares and details the importance⁶ of the flare as well as the beginning, maximum and end time of the emission. The time history of the whole Sun in soft (1–8 Å band⁷) X-rays as observed by the Geostationary Operational Environmental Satellites (*GOES*) is obtained from the Space Physics Interactive Data Resource (SPIDR) Web site⁸, maintained by the National Geophysical Data Center. The SPIDR interface is designed to allow the user to specify the desired *GOES* station, the energy range of observation (1–8 Å or 0.5–4 Å) and the time interval (data available from 01-01-1986 to 31-01-2008 with a minimal 1 min time resolution). We also include hard X-ray flux profiles measured by the Hard X-ray Telescope (HXR; Kosugi et al. 1991) on board *Yohkoh* and by the Reuven Ramaty High-Energy Solar Spectroscopic Imager (*RHESSI*; Lin et al. 2002), whenever available. Data is at 0.5 s and 4 s time resolution, and it is integrated over the energy ranges 33–53 keV and 25–50 keV, respectively. Data from *Yohkoh* and *RHESSI* have

⁴http://www.srl.utu.fi/erne_data/datafinder/df.html

⁵<http://sgd.ngdc.noaa.gov/sgd/> (US DoC: US Department of Commerce, Boulder, CO, USA).

⁶The importance of a soft X-ray flare, that is the X-ray class, is assigned based on the value of the peak intensity of the soft X-ray emission of the Sun in the 1–8 Å band. The class of an X-ray flare is given by a letter (A, B, C, M or X) accompanied by a certain numeric value. The numeric values (in units of W m⁻²) of the letter classes are: A = 10⁻⁸, B = 10⁻⁷, C = 10⁻⁶, M = 10⁻⁵ and X = 10⁻⁴. The intensity of a C5.9 flare, for example, is 5.9 × 10⁻⁶ W m⁻².

⁷Soft X-ray flux from 1–8 Å is a combination of continuum and line contributions, produced by free-free bremsstrahlung, free-bound recombination and two-photon emission. In the range 1–8 Å, the soft X-ray flux is dominated by contributions from the hot corona (> 10⁶ K), while contributions from the cooler parts of the corona are negligible. Thus, the solar 1–8 Å flux is believed to originate from heated plasma confined in closed magnetic loops in active regions (Aschwanden 1994).

⁸<http://spidr.ngdc.noaa.gov/spidr/>

been provided by S. Pohjolainen (2008, private communication).

In addition, we use white light observations of CMEs from LASCO (Brueckner et al. 1995). The *SOHO/LASCO* CME catalog⁹ has provided monthly lists of manually identified CMEs since 1996. Each CME is identified by attributes such as the time of the first appearance in the C2 coronagraph, the position angle (measured counterclockwise from the conventional solar north), the plane-of-sky speed of the leading-edge and the width of the CME, among others. The CME catalog is maintained by NASA and The Catholic University of America in cooperation with the Naval Research Laboratory. The estimation of the CME parameters is made by S. Yashiro and G. Michalek.

Finally, we also utilize radio data acquired by the WAVES experiment on the *Wind* spacecraft (Bougeret et al. 1995). WAVES measures radio emission in three different spectral regions by means of three receivers: RAD2 (13825–1075 kHz), RAD1 (1040–20 kHz), and TNR (256–4 kHz). One minute averages of the RAD1, RAD2, and TNR measurements are available from the *Wind/WAVES* web page¹⁰ in ASCII (compressed) and idl *save* format (.sav). The IDL software that allows to *restore* the .sav files and plot the radio dynamic spectra is also available online. For our purposes, we use data recorded by the RAD1 and RAD2 receivers.

2.4 Modeling sectorized intensities

2.4.1 Definition of the sectors

A particle detector on board a spin-stabilized spacecraft sweeps out a sample of space as the spacecraft spins. Every spin period, the swath of space scanned by the detector is divided into equally spaced regions called sectors. The set of measurements attributed to the sectors constitute the observation made by the telescope.

Gold et al. (1998) identified the sectors of the LEFS60 telescope by the zenith direction, \hat{s} , of the detector at the midpoint clock angle of each sector. Thus, in the spacecraft coordinate system, the view vectors point 60° from the spacecraft spin axis and they are separated from each other a multiple of 45° in clock-angle. Table 2.3 shows the definition of the LEFS60 sectors according to Gold et al. (1998). The first column identifies the sector with a letter and the two following ones give the polar angle and the clock-angle of the view vector associated with each sector in the spacecraft reference frame. On the other hand, in the EPAM processing software, sectors are defined by the direction of incidence of the particles observed by

⁹http://cdaw.gsfc.nasa.gov/CME_list/

¹⁰<http://www-lep.gsfc.nasa.gov/waves/waves.html> (maintained by M. L. Kaiser).

Table 2.3: Definition of the sectors of the LEFS60 telescope.

Gold et al. (1998)			EPAM software		
Sector	\hat{s}		$-\hat{s}$		Sector
ID	θ	ϕ	θ	ϕ	ID
a	60°	67.5°	120°	247.5°	6
b	60°	112.5°	120°	292.5°	7
c	60°	157.5°	120°	337.5°	8
d	60°	202.5°	120°	22.5°	1
e	60°	247.5°	120°	67.5°	2
f	60°	292.5°	120°	112.5°	3
g	60°	337.5°	120°	157.5°	4
h	60°	22.5°	120°	202.5°	5

each sector. Note that particles observed when the detector has a zenith direction \hat{s} , have an incident direction $-\hat{s}$. The fourth and fifth column in Table 2.3 list the polar and clock-angle of the incident direction of the particles associated with each sector. The last column lists the number with which each sector is identified in the EPAM processing software.

2.4.2 Pitch-angle distributions

The particle pitch-angle cosine, μ , is defined as the cosine of the angle between the particle velocity and the magnetic field vector and it is given by the scalar product of the unit magnetic field vector and the unit velocity vector of the particle; thus, $\mu = \hat{B} \cdot \hat{v}$.

The angle that the average magnetic field unit vector, \hat{B} , makes with respect to the zenith direction of the detector at the midpoint clock angle of the sector is normally related to the pitch-angle of the particles being scanned. That is, the pitch-angle cosine, μ , of the particles being observed by the detector at the midpoint clock angle the sector, is given by

$$\mu = -\hat{B} \cdot \hat{s} \quad (2.1)$$

Hereafter we will refer to this value of μ as the pitch-angle cosine of the particles scanned by the sector. Note however, that this definition is a simplification because the detector scans particles in a range of pitch-angle cosines as (1) it has a view-cone aperture of 53°, and (2) it spins to sweep out the sample of space attributed to the sector.

The extent to which sectorized measurements map out in pitch-angle depends on the direction of the magnetic field with respect to the spacecraft axis. For example, if the magnetic field were to be aligned with the spin axis, then all sectors would view exactly the same range in pitch-angle cosine and the observations would have little value in the analysis of the pitch-

angle distribution (PAD) of the measured particles. Because of the orientation of the EPAM telescopes and the orientation of the *ACE* spin axis, this is rarely the case.

The most extended procedure to represent PADs from a set of sectorized intensities consists in plotting, for a given time interval, the measured sectorized intensities against the inferred pitch-angle cosine of the sectors. For a given time interval, the magnetic field vector and the number of counts in each sector are averaged. As an example, Figure 2.2 displays the electron intensities observed on 2000 February 18 by the eight sectors of the EPAM/LEFS60 telescope in the E'1 energy channel and for a given time interval (adapted from Haggerty & Roelof 2002). For each sector (labeled by numbers), the cosine of the sector pitch-angle is plotted on the abscissa, and the intensity (normalized to the maximum) is plotted on the ordinate. Note that this kind of plot does not include information on the range of pitch-angle cosines covered by each sector.

PADs can also be described in terms of an expansion of orthogonal Legendre functions as

$$F(\mu) = \sum_{i=0} A_i P_i(\mu) = A_0 + A_1 \mu + \dots \quad (2.2)$$

In this Legendre polynomial expansion, the first (A_0) and the second (A_1) terms are given by

$$A_0 = \frac{1}{2} \int_{-1}^{+1} F(\mu) d\mu \quad (2.3)$$

$$A_1 = \frac{3}{2} \int_{-1}^{+1} \mu F(\mu) d\mu. \quad (2.4)$$

The isotropic part of the PAD is given by A_0 . The first-order anisotropy of the particle distribution is defined as the quotient between the second and the first term of the Legendre polynomial expansion (A_1/A_0). The ratio between these two terms is related to the average mean pitch-angle cosine since

$$\langle \mu \rangle = \frac{\frac{1}{2} \int_{-1}^{+1} \mu F(\mu) d\mu}{\frac{1}{2} \int_{-1}^{+1} F(\mu) d\mu} = \frac{\frac{1}{3} A_1}{A_0} \quad (2.5)$$

Therefore, the first-order anisotropy is given by

$$\frac{A_1}{A_0} = 3 \langle \mu \rangle \quad (2.6)$$

The first and second terms of the Legendre polynomial expansion can be evaluated using a

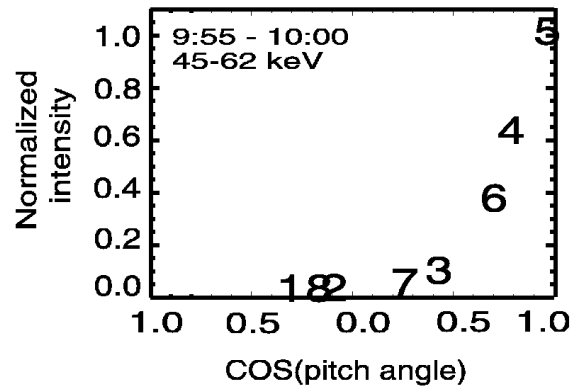


Figure 2.2: PAD with the pitch-angle cosine on the horizontal axis and the normalized intensity on the vertical axis. Each number (1–8) gives the intensity observed in each one of the eight sectors of the LEFS60 telescope normalized to the sector with maximum intensity. Energy range and accumulation interval at the top of the PAD (from Haggerty & Roelof 2002).

least squares fitting technique for a set of sectorized measurements of the particle intensity, assuming that $F(\mu)$ is the intensity measured by each sector, and μ the pitch-angle cosine attributed to each sector.

Figure 2.3 shows an example of the average anisotropy inferred from the electron intensities measured by EPAM in the 178–290 keV energy range on 2001 April 15. Note that the first-order anisotropy gives information related to the mean pitch-angle cosine of the observed particles and not regarding the overall particle distribution.

The methods explained above simplify the information contained in a set of sectorized data and therefore, do not reflect all the angular information it contains. Sometimes this simplification can be very helpful and can provide an estimation of the main direction of the flow. Nevertheless, if we aim to infer the transport conditions of NR electrons in the IP medium as well as the injection profile of particles close to the Sun by comparing observational sectorized intensities with PADs from a simulation, we need to model the angular response of the sectors scanned by a particle detector on board a spin-stabilized spacecraft. The next sections deal with this problem and provide an algorithm to transform simulated PADs into sectorized intensities that can be directly compared with observations.

2.4.3 Angular response model of sectors

In order to model the sectorized data collected by the LEFS60 telescope of the EPAM experiment (Gold et al. 1998), it is necessary to derive the angular response function of the sectors of the telescope. We have developed a model that includes the essential parts of the geometry of the detector system; but it does not take into consideration other factors such as the effects

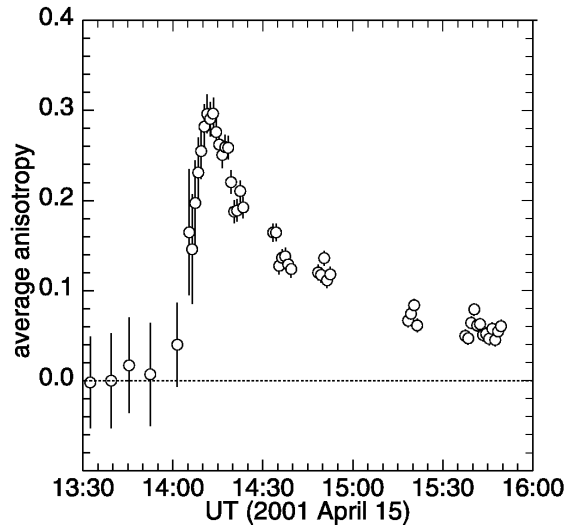


Figure 2.3: First-order anisotropy derived from 1 min 178–290 keV electron intensities measured in the different sectors of the EPAM experiment (from Maia et al. 2007).

of electron scattering in the collimated aperture. The angular response can be obtained by analyzing how an isotropic population of particles is seen by each one of the eight sectors of the LEFS60 telescope.

We take X, Y, Z as the coordinate system where the Z axis is aligned with the ACE spin vector and X and Y axes are perpendicular to it, maintaining constant orientation with respect to the ecliptic plane. The clock-angle, ϕ , is the azimuth angle measured around Z from the positive X toward the positive Y , and the spin-pitch angle, ξ , is the polar angle of this coordinate system. We refer to the coordinate system of the detector as X', Y', Z' , where the Z' axis is oriented toward the zenith direction of the detector. Figure 2.4 illustrates these two coordinate systems. As the spacecraft spins, the zenith direction changes at constant angular velocity with an uniformly increasing clock angle $\phi_0(t) \propto t$ and a constant spin-pitch angle $\xi_0 = 60^\circ$. The azimuth angle in this system, ϕ' , is measured around the Z' axis from the positive X' toward positive Y' and the polar angle, ξ' , is the zenith angle of a particle incident on the detector.

We model the LEFS60 detector as a conical aperture with an effective view-cone half-width of $\xi'_{\max} = 25^\circ$, mounted on a spinning spacecraft with a zenith direction given by a spin-pitch angle of $\xi_0 = 60^\circ$. In fact, the view cone of LEFS60 has a full width of 53° , but we use a slightly smaller value because the response in a real collimated aperture decreases over a range of zenith angles, instead of abruptly going to zero at the edge.

The response function R_{jk} of each sector is represented by a bi-dimensional matrix, where each element (j, k) represents the probability per square degree that a particle with direction (ξ, ϕ) is detected when the zenith axis of the detector sweeps a 45° -wide clock angle sector.

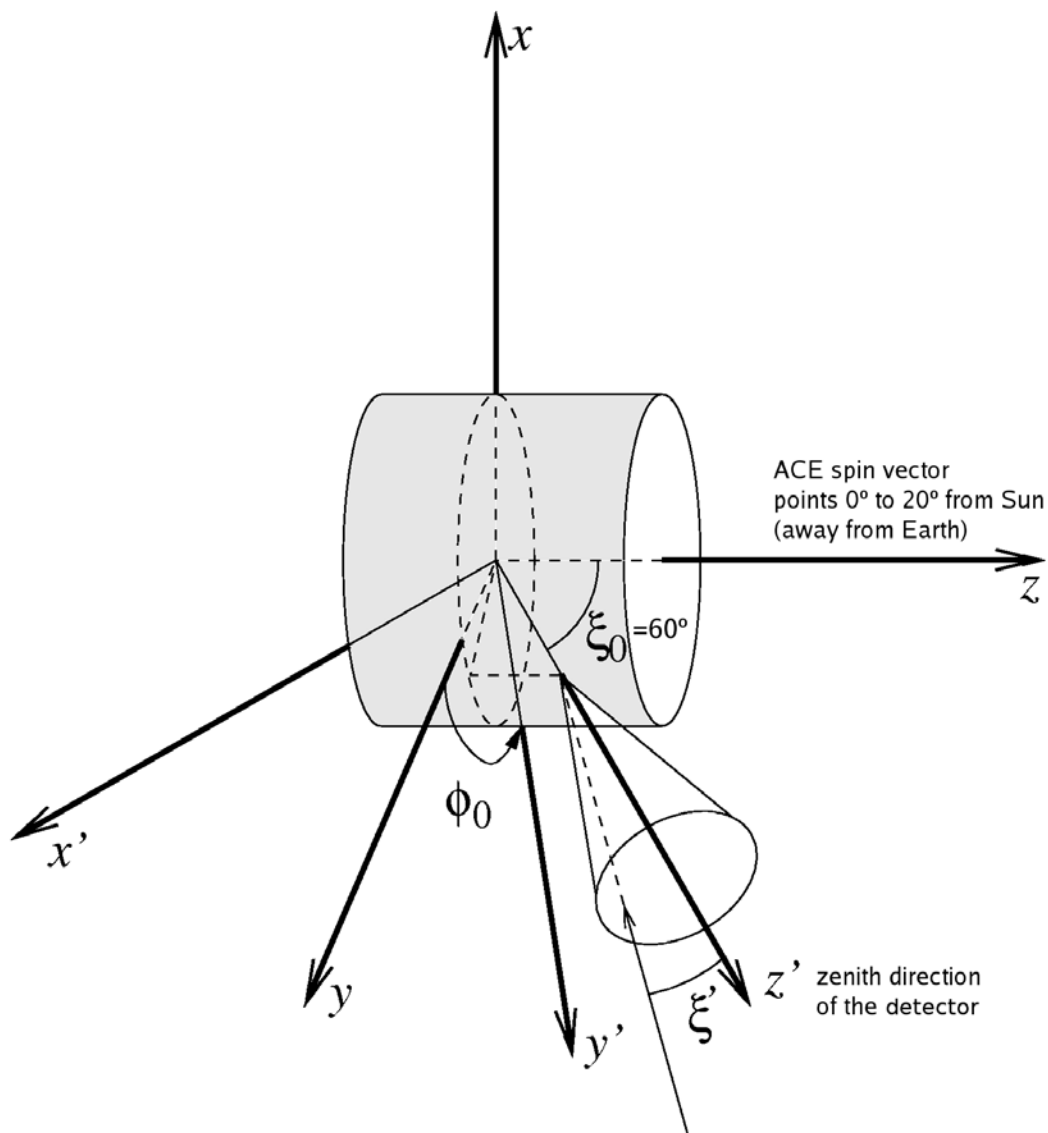


Figure 2.4: Coordinate systems: X, Y, Z denote the coordinate system where Z is aligned with the ACE spin vector and X and Y axes are perpendicular to it. The spin-pitch angle, ξ , is the polar angle of this coordinate system. X', Y', Z' denote the coordinate system of the LEFS60 detector. The Z' axis is oriented toward the zenith direction of the LEFS60 detector ($\xi_0 = 60^\circ$). See text for details.

If $(\xi, \phi) \in [j\alpha, (j+1)\alpha] \times [k\alpha, (k+1)\alpha]$, with $\alpha = 1^\circ$, and we take $\xi \in [0^\circ, 180^\circ]$ and $\phi \in [0^\circ, 360^\circ]$, this means that $j \in [0, 179]$ and $k \in [0, 359]$. Thus, R_{jk} is a 180×360 matrix.

We start by simplifying the problem and calculating the response function of a sector centered at $(\xi_0, \phi_0) = (60^\circ, 0^\circ)$. Assuming a non-rotating detector, we generate a large number of isotropic particle trajectories incident on the detector¹¹. We take the squared zenith angle cosines, $\cos^2 \xi'_i$, uniformly distributed between the squared cosine of the view-cone half-width, $\cos^2 \xi'_{\max}$, and 1, and the azimuth angles ϕ'_i uniformly distributed between 0 and 2π . The subscript i identifies the generated trajectories. For each trajectory (ξ'_i, ϕ'_i) , we then calculate the spin-pitch angle of the trajectory, ξ_i , which is given by

$$\cos \xi_i = \sin \xi_0 \sin \xi'_i \cos \phi'_i + \cos \xi'_i \cos \xi_0 \quad (2.7)$$

and the respective clock-angle, ϕ_i , by

$$\sin \phi_i = \frac{\sin \xi'_i}{\sin \xi_i} \sin \phi'_i. \quad (2.8)$$

The next step is to take into account the sampling of clock-angle of the detector-zenith direction as the spacecraft spins. We do this by adding to the clock-angle ϕ_i a random number uniformly distributed between $(-\delta\phi/2, \delta\phi/2)$ with $\delta\phi = 45^\circ$. The result is a set of particle trajectories drawn from an isotropic particle distribution, as seen by the detector when its zenith axis sweeps a 45° -wide clock angle sector centered at $\phi_0 = 0^\circ$.

We create the response matrix R_{jk} of the sector by binning the particle trajectories (ξ_i, ϕ_i) on the matrix R_{jk} and normalizing to unity, $\sum_{jk} R_{jk} = 1$. Figure 2.5 illustrates the response function of this sector. Note that it is not a boxcar function, but it peaks at the midpoint clock-angle zenith direction of the sector.

Finally, the response function of each of the eight sectors of the EPAM/LEFS60 telescope can be easily derived by shifting R_{jk} in clock-angle, taking into account that the midpoint clock-angle of the first sector is located at 67.5° and it is separated a multiple of 45° from the neighboring sectors (Gold et al. 1998).

¹¹An isotropic particle population incident on a detector follows a cosine distribution; $P(\mu) = 2\mu$ and $\int_0^1 P(\mu) d\mu = 1$. To sample this distribution we use the equation $\int_0^\mu P(\mu) d\mu = \zeta$, where ζ is a random uniform variable on $(0, 1)$. Integrating we obtain that $\mu^2 = \zeta$, that is, the squared cosines follow a uniform distribution.

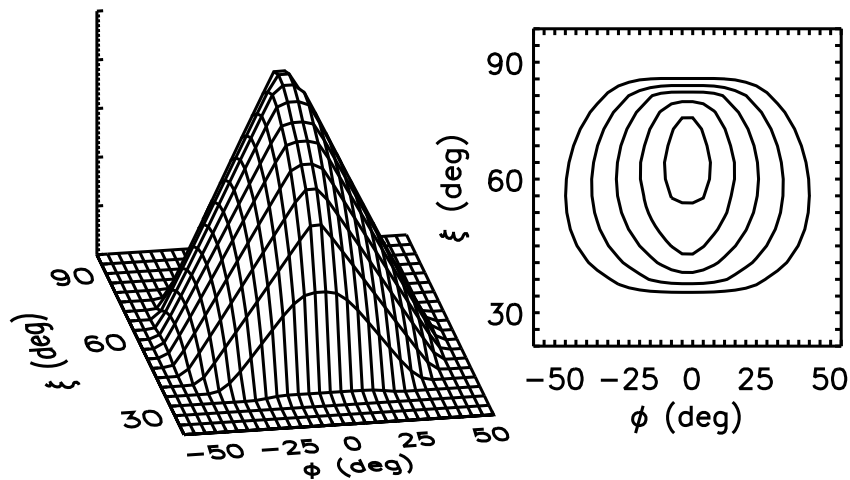


Figure 2.5: Bidimensional response function for a sector characterized by a midpoint clock-angle of 0° , a view cone full-width of 50° , a clock-angle sector size of 45° , and a spin-pitch angle of 60° . Surface plot (left) and contour diagram (right).

2.4.4 View boundaries

If we relate the direction of incidence of the particles to the local direction of the magnetic field we can derive the range of pitch-angle cosine scanned by each sector. This is important to understand to what extent the data computed by the telescope maps the PAD. Note that the most conclusive studies about the transport and injection history of NR electrons can only come from those events observed with a high coverage of PADs.

Figure 2.6 illustrates the solid angle encompassed by LEFS60 in the spacecraft coordinate system. The Z axis is the spin axis of the spacecraft and the X and Y axes are perpendicular to it. The solid angle encompassed by the telescope is constant in the spacecraft coordinate system and it is divided in eight equal sectors (labeled with letters). However the range of pitch-angle cosines scanned by the telescope depends on the magnetic field direction. We define a generic magnetic field vector in the spacecraft coordinate system, given by the unit vector $\hat{B} = (1, \theta_B, \phi_B)$ expressed in spherical coordinates (θ_B is the polar angle and ϕ_B is the clock-angle). From the figure, it is clear that a change in θ_B produces a change in the range of μ scanned by the telescope. Whereas a change in ϕ_B , modifies the range of μ scanned by each sector but it does not change the range of μ scanned by the telescope (consisting of all sectors).

Using the same grid of directions (ξ, ϕ) as for the calculation of R_{jk} , we can calculate the matrix of pitch-angle cosines, $\mu_{jk} = \mu(\xi_j, \phi_k, \hat{B})$, taking into account the orientation of the magnetic field vector. If R_{jk}^s is the response matrix corresponding to sector s , the response of sector s as a function of μ is derived by binning the (μ_{jk}, R_{jk}^s) data points according to μ

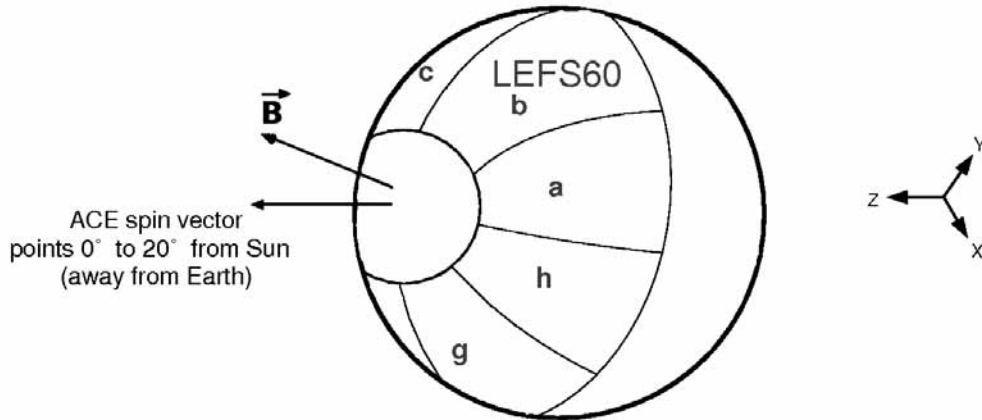


Figure 2.6: Solid angle encompassed by the LEFS60 telescope projected onto a sphere. Generic magnetic field vector in the spacecraft coordinate system, where Z is the spin axis and X , Y complete the perpendicular triad.

and weighting according to R_{jk}^s . Figure 2.7 illustrates the response of each sector in μ for two different magnetic field configurations: one with $\theta_B = 0^\circ$ and one with $\theta_B = 90^\circ$ for $\phi_B = 60^\circ$, respectively. In the first case ($\theta_B = 0^\circ$), the magnetic field vector is aligned with the spin axis of the spacecraft and as a consequence all sectors scan the same range in pitch-angle cosine. On the other hand, when $\theta_B = 90^\circ$, all sectors scan a different range in μ and the telescope (composed by all sectors) covers all the possible values of μ .

To derive the view boundaries of the sector, that is, the highest and the lowest μ values scanned by the sector, we extract the maximum and the minimum μ values of the μ_{jk} matrix that have a non zero response. The highest and the lowest μ values from all of the sectors are then the maximum and the minimum μ values scanned by the telescope.

Using this procedure, we can calculate the view boundaries of each sector as a function of the magnetic field configuration. We take $\theta_B \in [0^\circ, 180^\circ]$ and ϕ_B constant. Figure 2.8 shows two examples, with $\phi_B = 45^\circ$ and $\phi_B = 60^\circ$ respectively. Each color represents one of the sectors of the LEFS60 telescope. For each sector there are two lines: one for the highest and another one for the lowest μ value scanned by each sector as a function of θ_B . As expected, when $\theta_B = 0^\circ$ or $\theta_B = 180^\circ$ all sectors scan the same range in μ . When $\phi_B = 45^\circ$ and $\theta_B \in [0^\circ, 180^\circ]$, pairs of sectors have the same view boundaries because the magnetic field vector lays in the frontier between two sectors. When $\phi_B = 60^\circ$ the range of μ values scanned by each sector is different. Note, however, that the pitch-angle cosine range covered by the telescope, only depends on θ_B because the system is symmetric with respect to ϕ . For $\theta_B = 90^\circ$ the telescope scans almost all the possible values of μ .

We define the pitch-angle cosine coverage of the telescope, μ -co, as the percentage of the

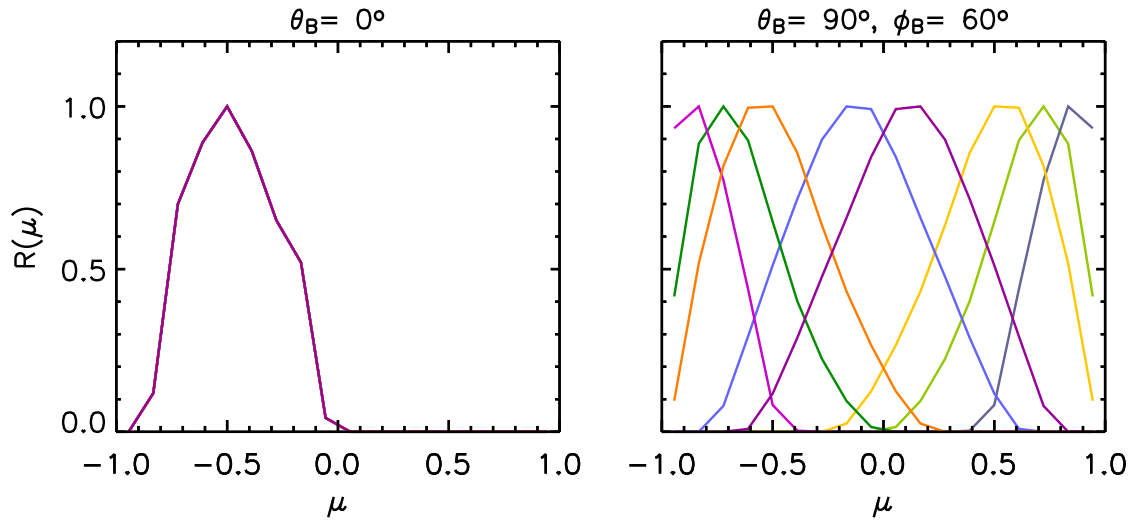


Figure 2.7: Response function (normalized to maximum) of the eight sectors of the LEFS60 telescope for $\theta_B = 0^\circ$ (left) and $\theta_B = 90^\circ$ (right) with $\phi_B = 60^\circ$. Different colors represent different sectors. In the case with $\theta_B = 0^\circ$, all sectors scan the same range of μ .

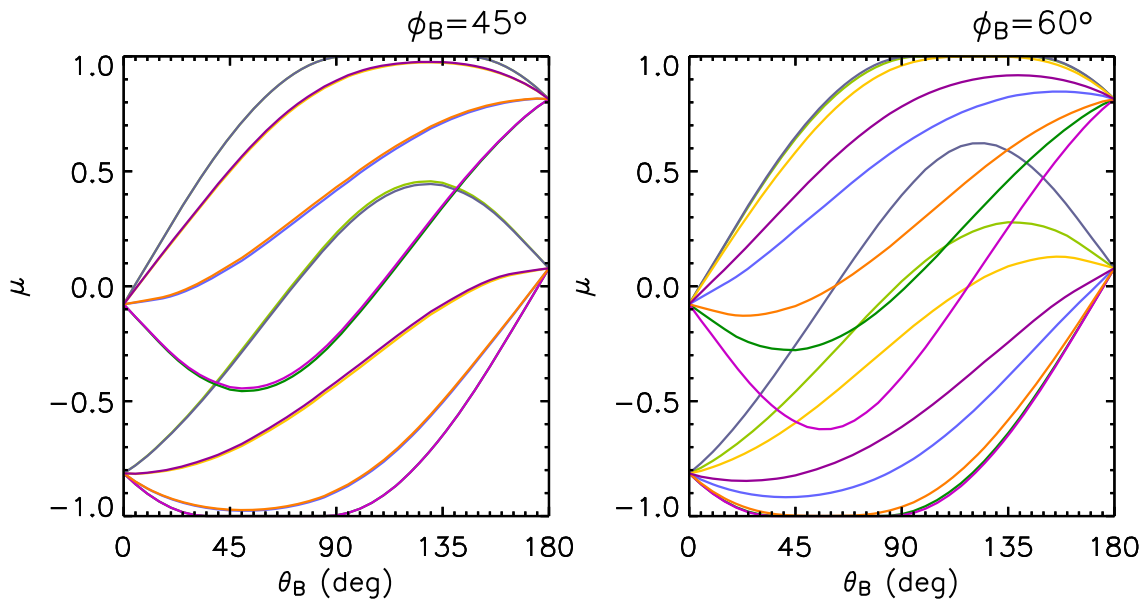


Figure 2.8: View boundaries of the sectors of the LEFS60 telescope (different colors represent different sectors) as a function of the magnetic field direction, where $\theta_B \in [0^\circ, 180^\circ]$ for $\phi_B = 45^\circ$ (left) and $\phi_B = 60^\circ$ (right).

pitch-angle cosine range scanned by the telescope for a given magnetic field configuration. Thus,

$$\mu\text{-co}(\%) = \frac{1}{2}(\mu_{\max} - \mu_{\min}) \times 100 \quad (2.9)$$

where μ_{\max} and μ_{\min} are the highest and the lowest μ values observed by the telescope.

Figure 2.9 (top) shows the pitch-angle cosine range covered by the LEFS60 telescope as a function of θ_B and the μ -co for each case. The lowest μ -co provided by the LEFS60 telescope is below 40% and it corresponds to the cases $\theta_B = 0^\circ$ and $\theta_B = 180^\circ$. The μ -co $\approx 100\%$ is achieved when $\theta_B = 90^\circ$; only in this case the LEFS60 telescope is able to observe almost the complete pitch-angle cosine range.

It is possible to use the algorithm developed for the study of the sectorized data measured by the LEFS60 telescope to other telescopes on board *ACE*. For example, we can calculate the angular response of the sectors of the LEMS30 telescope by assuming $\xi_0 = 30^\circ$ and $\delta\phi = 90^\circ$. Figure 2.9 (bottom) shows the pitch-angle cosine range covered by the LEMS30 telescope as a function of θ_B and the μ -co for each case. In this case, the μ -co of the telescope ranges from 20% to 80%. Therefore, from the point of view of the μ coverage, the LEFS60 telescope is more appropriate for data analysis than the LEMS30.

Finally, note that if the magnetic field vector remains stable during the evolution of an SEP event, the μ -co of the telescope is constant throughout the event. The magnetic field vector, however, does normally vary with time. Therefore, we define the μ -co of the telescope for a given SEP event as the mean of the μ -co values obtained for each time interval under study.

2.4.5 Sectorized Green's functions

Once we know the angular response function of the sectors of the LEFS60 telescope, it is possible to transform simulated differential intensities into modeled sectorized intensities, which are directly comparable with observations. Note that the μ_{jk} matrix will normally change as a function of time due to the change of direction of the magnetic field vector, $\hat{B}(t)$. From this $\mu_{jk}(t)$ matrix, we can calculate the corresponding angular distribution $G_l(\mu_{jk}(t), t)$, where $G_l(\mu, t)$ are the simulated pitch-angle distributions in the energy range $[E_l, E_l + \Delta E_l]$ resulting from an impulsive injection at $t = 0$. In this case, the modeled intensities in sector s and energy channel l are given by

$$g_l^s(t) = \sum_{jk} R_{jk}^s G_l(\mu_{jk}(t), t); \quad (2.10)$$

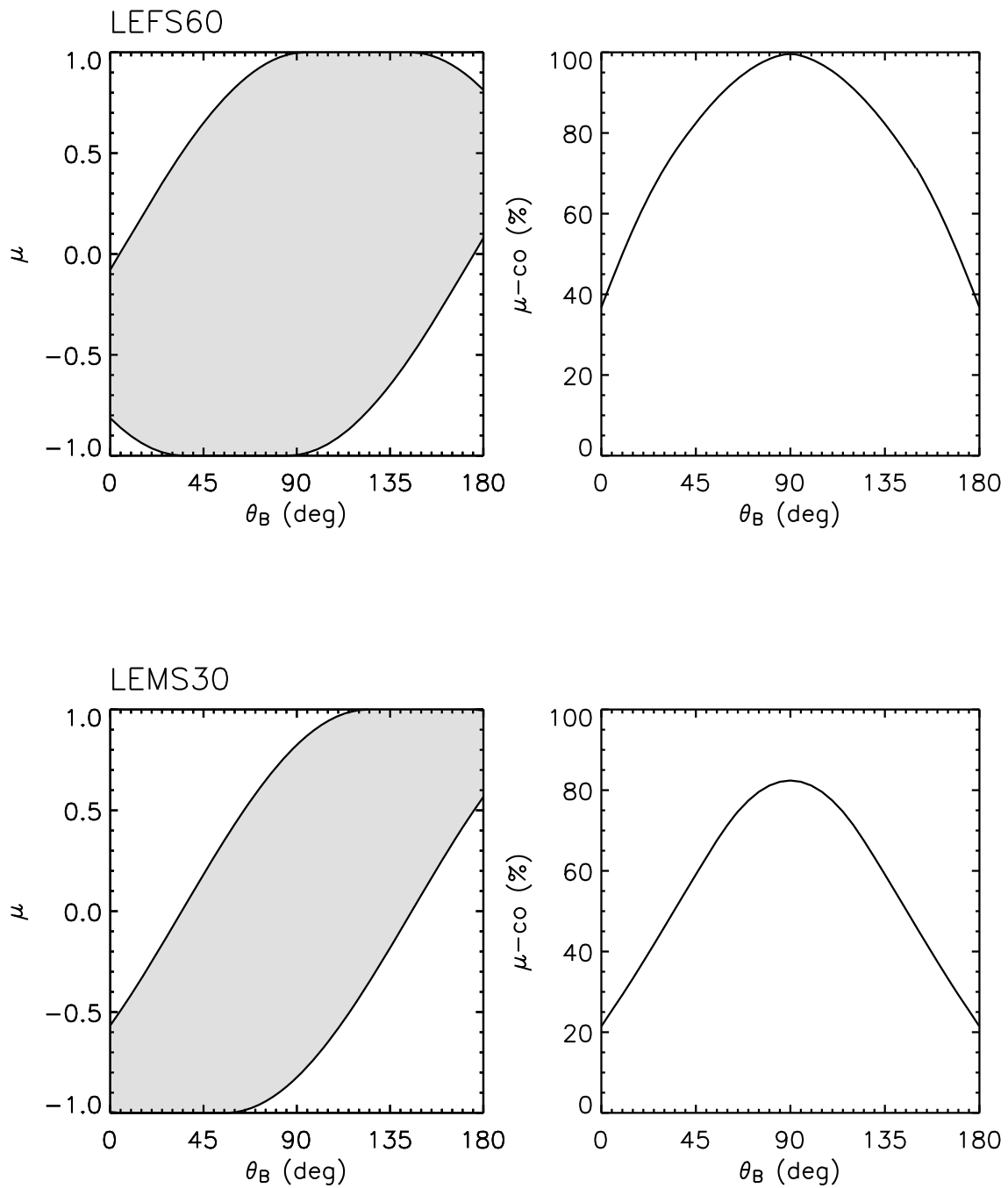


Figure 2.9: Pitch-angle cosine range covered by the LEFS60 (top) and the LEMS30 (bottom) telescopes as a function of the polar angle, θ_B , of the magnetic field vector (left). Pitch-angle cosine coverage (μ -co) of the telescope for each case (right).

i.e. the product is performed element by element and the sum extends over all (ξ, ϕ) directions.

In general, we can write

$$g_l^s(t, t') = \int_0^\pi d\xi \int_0^{2\pi} d\phi R^s(\xi, \phi) \frac{1}{\Delta E_l} \int_{E_l}^{E_l + \Delta E_l} dE G(\mu(\xi, \phi, t), t - t', E), \quad (2.11)$$

where $g_l^s(t, t')$ represents the modeled intensity, for a given sector s and energy channel l , at a given time t , when the injection of particles took place at time t' .

2 INSTRUMENTATION AND DATA ANALYSIS